American Mineralogist, Volume 95, pages 1458–1466, 2010

Kinetics of Fe-oxidation/deprotonation process in Fe-rich phlogopite under isothermal conditions

MICHELE ZEMA,[1,2] GENNARO VENTRUTI,[3] MARIA LACALAMITA,[3] AND FERNANDO SCORDARI[3,*]

[1]Dipartimento di Scienze della Terra, Università degli Studi di Pavia, via Ferrata 1, I-27100 Pavia, Italy
[2]CNR-IGG, Sezione di Pavia, via Ferrata 1, I-27100 Pavia, Italy
[3]Dipartimento Geomineralogico, Università degli Studi di Bari, Via E. Orabona 4, I-70125 Bari, Italy

ABSTRACT

The kinetics of the Fe-oxidation/deprotonation process in a natural Fe-rich phlogopite from Mt. Vulture (Potenza, Italy) was studied under isothermal conditions by in situ high-temperature single-crystal X-ray diffraction. Isothermal annealing experiments were performed at five temperatures in the range 640–750 °C on five crystals with similar chemical composition and lattice parameters. The Fe-oxidation/deprotonation process at high temperature occurs with a reduction of unit-cell parameters and cell volume. The changes in unit-cell parameters measured at high temperature and during cooling show that the same degree of Fe-oxidation/deprotonation process was achieved at all temperatures. Changes in unit-cell parameters with temperature and time show that the kinetics of Fe-oxidation/deprotonation in phlogopite follows an exponential law, and the temperature dependence follows the Arrhenius relation. A kinetic analysis was performed and good agreement was obtained with the one-dimensional diffusion model. An apparent activation energy of 195(4) kJ/mol was determined.

Keywords: Trioctahedral mica, kinetics, deprotonation, single-crystal X-ray diffraction, high temperature

INTRODUCTION

Water plays a fundamental role in many geological processes. For example, water is reintroduced in the Earth's mantle during subduction. Release of water during subduction is responsible for metasomatism and partial melting of the overlying mantle wedge, and associated volcanic activity at the surface. The behavior of hydrous mineral phases (capable of storing water in their structures as OH^- or H_2O) under different physical-chemical conditions is important to understand the structural mechanisms and rates at which water is released.

Micas are common rock-forming phases, present in a great variety of geological environments and involved in many petrogenetic reactions occurring in fluid-absent melting processes (Vielzeuf and Schmidt 2001) and in mineral-fluid interactions (Zeng et al. 1990). Micas contribute significantly to the storage and release of water in the mantle through complex reactions (Virgo and Popp 2000). Nevertheless, although detailed information is present regarding how mica crystal structures respond to temperature (Brigatti and Guggenheim 2002; Zanazzi and Pavese 2002 and references therein), few data exist on the kinetics of the dehydration process. Previous studies emphasize dioctahedral micas, where a "pure" dehydroxylation process occurs: two hydroxyl groups belonging to a coordination octahedron are replaced by one residual O atom and a molecule of H_2O is released (e.g., Guggenheim et al. 1987), thus producing a change in coordination from six to five about the Al cations. The kinetics of dehydroxylation in muscovite was studied by several techniques. Mazzucato et al. (1999) and Tokiwai and Nakashima (2010) proposed that the process is rate-limited by mono-dimensional diffusion along **c*** and determined an activation energy of ~251 and ~290 kJ/mol, respectively.

The Fe-bearing trioctahedral micas undergo a simple deprotonation process, before dehydroxylation at near 1100 °C (Vedder and Wilkins 1969). This process is controlled by Fe-oxidation, i.e., Fe^{2+} cations in the octahedral sheet are oxidized to Fe^{3+} and one H atom is released. The redox reaction is written as: $(Fe^{2+}+OH^-)_{mica} \leftrightarrow (Fe^{3+}+O^{2-})_{mica} + ½H_2\uparrow$, and the direction of the reaction contributes to the uptake and release of hydrogen. Deprotonation in Fe-bearing trioctahedral micas was investigated by Tsvetkov and Val'yashikhina (1956), who analyzed biotite in an inert atmosphere at 500–900 °C. Mössbauer and infrared spectroscopies examined changes in the local and electronic environment of hydroxyl groups and in the oxidation state of octahedral Fe cations. Oxidation of Fe^{2+} to Fe^{3+} occurs in biotite with simultaneous loss of hydrogen at T ~400 °C in air (Vedder and Wilkins 1969; Hogg and Meads 1975), and is delayed by the under-stoichiometry of O_2 in vacuum (Sanz et al. 1983). Ferrow (1987) observed that *cis* sites (M2) oxidize more readily than *trans* sites (M1) in synthetic annite and ferriannite. Diffraction techniques were used to investigate structural changes and phase transitions induced by heat treatment on Fe-bearing natural and synthetic trioctahedral micas, and particularly on phlogopite. After studies on synthetic fluorophlogopite (Takeda and Morosin 1975), reduced and hydrogenated biotite (Takeda and Ross 1975), and oxidized (oxy-mica) and hydrogen-depleted (Ohta et al. 1982) Fe-rich phlogopite polytypes, Russell and Guggenheim (1999) determined the crystal structure at various

* E-mail: f.scordari@geomin.uniba.it

temperatures and measured the thermal expansion of interlayer and octahedral sites of several phlogopite crystals by single-crystal X-ray diffraction.

Deprotonation decreases the interlayer separation, owing to the reduced electrostatic repulsion between the interlayer cation and H, and reduces the octahedral sheet dimensions because of the decrease in radius of Fe resulting from the change in oxidation state. Consequently, the deprotonation process is accompanied by a decrease of unit-cell parameters and volume. These changes were observed by Tutti et al. (2000) by high-temperature (HT) X-ray powder diffraction and thermogravimetry and derivative thermogravimetry (TGA-DTG) at 500–600 °C and by Chon et al. (2003, 2006), who combined in situ HT neutron powder diffraction with ex situ HT Fourier-transform infrared (FTIR) spectroscopy. Ventruti et al. (2008) analyzed the structural changes of Fe-rich phlogopite at 100–1023 K by single-crystal X-ray diffraction and characterized the effects of thermal expansion and deprotonation. They observed a small change in the thermal expansion of protonated and deprotonated samples. The position of the hydrogen atom and hence the orientation of the hydroxyl group in phlogopite were accurately determined by neutron powder diffraction at 10 K by Ventruti et al. (2009). They also modeled the deviation from linearity of thermal expansion at low temperatures by an Einstein expression based on Grüneisen's rule.

With regard to the kinetics of deprotonation in trioctahedral micas, Rouxhet (1970) showed that diffusion of protons along the **c*** axis in phlogopite is similar to diffusion in muscovite during dehydroxylation. Comodi et al. (1999) performed a qualitative study of the kinetics of deprotonation on a synthetic Cs-tetra-ferriannite single crystal. They found that a decrease of unit-cell parameters measured at 582 °C as a function of time follows two patterns, and suggested that iron oxidation occurs initially at the M2 site and, subsequently, at the M1 site, which causes damage to the crystal structure. Rancourt et al. (1993) performed a kinetic study of iron oxidation in biotite by quantifying the Fe^{2+}/Fe^{3+} ratio after heat treatments in air at various temperatures and for various times by Mössbauer spectroscopy. An apparent activation energy of 228 kJ/mol was determined, close to the non-diffusion energy barrier measured for dehydroxylation of kaolinite (Redfern 1987). Rancourt et al. proposed, by analogy, that the local dissociation of the OH^- group ($OH^- \rightarrow O^{2-}+H^+$) is the rate-limiting step of the overall reaction. The reaction mechanism of the dehydration process in kaolinite (Bellotto et al. 1995) and other minerals (Ingrin and Skogby 2000; Sundvall et al. 2009) was reinterpreted on the basis of a diffusion-controlled model.

In the present paper, we use a kinetic analysis of the deprotonation process of an Fe-bearing phlogopite by in situ high-temperature single-crystal X-ray diffraction. Isothermal data measured at five temperatures in the range 640–750 °C were modeled using a reaction mechanism limited by a mono-dimensional diffusion law.

Experimental methods

Samples

The high-temperature crystallographic study was performed on five Fe-Ti-rich phlogopite-1*M* crystals from Cava St. Antonio (Mt. Vulture, Italy), hereafter referred to as SA. Trioctahedral micas from the SA sample belong to the phlogopite-annite solid solution [$X_{Fe} = Fe_{tot}/(Fe_{tot}+Mg) \approx 0.25$] with Ti ≈ 0.20 atoms per formula unit (apfu) and are homogeneous in chemical composition and structural parameters (see Scordari et al. 2006; Ventruti et al. 2008). The selected crystals are similar in size (Table 1) and show negligible diffuse streaking parallel to **c***, which indicates stacking order.

Electron microprobe analyses

Three crystals were analyzed by electron microprobe before performing the HT experiments. Electron microprobe analyses (EMPA) were obtained with a Cameca SX-50 electron microprobe. The analyses were performed in wavelength dispersive (WDS) mode with operating conditions of 15 kV accelerating voltage, 15 nA beam current, 15 s peak count times, and 10 μm beam size. The standards used were: jadeite (Na), periclase (Mg), wollastonite (Si and Ca), rutile (Ti), corundum (Al), magnetite (Fe), orthoclase (K), barite (Ba), fluoro-phlogopite (F), and sylvite (Cl). Conversion from X-ray counts to oxide weight percentages (wt%) was obtained with the PAP data reduction method (Pouchou and Pichoir 1985). Chemical compositions are reported in Table 2, where atomic proportions are calculated on the basis of 12(O, OH, Cl, F) and by combining EMPA data with

Table 1. Crystal, experimental, and refinement data for 1*M* phlogopite samples

	SA1_9	SA1_5n	SA1_14n	SA1_15n	SA1_18n
Space group	*C*2/*m*	*C*2/*m*	*C*2/*m*	*C*2/*m*	*C*2/*m*
a (Å)	5.3379(3)	5.3388(2)	5.3403(2)	5.3435(2)	5.32568(8)
b (Å)	9.2414(5)	9.2464(3)	9.2481(4)	9.2530(5)	9.2207(1)
c (Å)	10.2311(6)	10.2365(4)	10.2327(4)	10.2458(5)	10.2093(2)
β (°)	100.023(4)	100.037(3)	100.017(3)	100.006(4)	100.014(1)
V (Å^3)	497.00(5)	497.59(3)	497.66(4)	498.88(5)	493.71(1)
Z	2	2	2	2	2
Crystal size (mm^3)	0.25 × 0.26 × 0.022	0.47 × 0.20 × 0.025	0.24 × 0.30 × 0.03	0.23 × 0.30 × 0.015	0.28 × 0.25 × 0.03
Crystal-detector distance (mm)	40	40	40	40	40
Rotation axes, width (°)	φ, ω, 0.5	φ, ω, 0.5	φ, ω, 0.5	φ, ω, 0.3	φ, ω, 0.5
Exposure time (s/°)	10	10	10	10	10
No. of frames	2094	1809	1809	3156	1809
θ range for data collection	4–45	4–44	2–44	4–44	4–44
Reflections measured/unique	20384/2102	18352/1999	18402/1991	18221/2010	18572/1998
R_{int}	0.080	0.033	0.0396	0.053	0.028
Reflections used	663 with $I > 3\sigma_I$	1170 with $I > 3\sigma_I$	1042 with $I > 3\sigma_I$	817 with $I > 3\sigma_I$	1271 with $I > 3\sigma_I$
No. of refined parameters	68	72	72	72	72
Goof*	1.000	1.012	0.990	1.011	1.048
R_1† (on *F*)	0.0401	0.0258	0.0285	0.0304	0.0209
wR_2‡ (on F^2)	0.0417	0.0292	0.0338	0.0359	0.0232
$(\Delta/\sigma)_{max}$	0.0162	0.0114	0.0157	0.0149	0.0116
$\Delta\rho_{min}$, $\Delta\rho_{max}$ (e/Å^3)	–1.38, 0.66	–0.38, 0.80	–0.38, 0.71	–0.42, 0.84	–0.36, 0.77

* Goodness-of-fit = $\{\Sigma[w(F_o^2 - F_c^2)^2]/(N - P)\}^{1/2}$, where *N* and *P* are the number of reflections and parameters, respectively.
† $R_1 = \Sigma[|F_o| - |F_c|]/\Sigma|F_o|$.
‡ $wR_2 = \{\Sigma[w(F_o^2 - F_c^2)^2]/\Sigma[w(F_o^2)^2]\}^{1/2}$, where $w = 1/[\sigma^2(F_o^2) + (xP)^2 + yP]$.

those of Mössbauer spectroscopy (Scordari et al. 2006) and SIMS measurements (Ottolini et al. 2009). The final formulae were obtained by allowing H_2O variations within 1–2 estimated standard deviations (e.s.d.) to obtain a full occupancy of octahedral cations.

Single-crystal XRD at room temperature

Each crystal was examined preliminarily by single-crystal diffraction at room temperature using a Bruker AXS APEX2 diffractometer equipped with a CCD detector and graphite-monochromatized Mo$K\alpha$ radiation (λ = 0.71073 Å). Operating conditions were 50 kV and 30 mA. For each measurement, three sets of 12 frames were acquired with 0.5° ϕ rotation and the results were used for the initial unit-cell determinations. The collection strategy was optimized by the Apex program suite (Bruker 2004a); the intensities of reflections in the entire Ewald sphere ($\pm h, \pm k, \pm l$) were recorded by a combination of ω and ϕ rotation sets with a 0.5° scan width. The package SAINT-IRIX (Bruker 2004b) was used for data reduction, including intensity integration; moreover the data were corrected for Lorentz, polarization, background effects and scale variation. The final unit-cell parameters were obtained from the *xyz* centroids of the measured reflections after integration and are reported in Table 1, together with details on data collection. A semi-empirical absorption correction based on the determination of transmission factors for equivalent reflections (Blessing 1995) was applied using SADABS software (Sheldrick 2004).

Each structure refinement was performed in space group *C*2/*m* using program CRYSTALS (Betteridge et al. 2003) starting from the data of Scordari et al. (2006).

TABLE 2. Electron microprobe analyses and atomic proportions (apfu) as determined by combining EPMA, Mössbauer, and SIMS analyses

	SA1_14n	SA1_18n	SA1_9
	wt%		
SiO_2	34.85(78)	35.06(42)	33.71(35)
TiO_2	3.50(9)	3.15(6)	3.47(6)
Al_2O_3	15.61(21)	15.71(18)	15.29(28)
Cr_2O_3	–	0.02(3)	0.02(2)
NiO	–	0.04(3)	–
FeO_{tot}	11.01(25)	11.01(5)	10.86(16)
MnO	0.18(5)	0.14(2)	0.17(3)
MgO	17.48(34)	18.62(16)	17.55(38)
BaO	1.68(25)	1.07(6)	1.75(12)
CaO	0.05(9)	0.01(1)	0.03(2)
Na_2O	0.49(4)	0.55(2)	0.44(3)
K_2O	8.51(10)	9.26(9)	8.55(11)
F	0.69(9)	0.69(9)	0.66(10)
Cl	0.04(1)	0.04(2)	0.04(2)
Total	94.09(1.16)	95.37(64)	97.36(19)
FeO*	4.84	4.84	4.69
Fe_2O_3*	6.86	6.86	6.65
H_2O†	2.60(6)	2.60(6)	2.60(6)
	apfu based on 12 (O, OH, F, Cl)		
Si	2.67	2.64	2.63
^{IV}Al	1.33	1.36	1.37
Σ	4.00	4.00	4.00
^{VI}Al	0.08	0.03	0.04
Mg	2.00	2.08	2.05
Fe^{2+}	0.31	0.30	0.31
Fe^{3+}	0.40	0.39	0.39
Ti	0.20	0.18	0.20
Mn	0.01	0.01	0.01
Cr	–	–	–
Ni	–	0.01	–
Σ	3.00	3.00	3.00
K	0.83	0.89	0.85
Na	0.07	0.08	0.07
Ba	0.05	0.03	0.05
Ca	–	–	–
Σ	0.95	1.00	0.97
OH	1.27	1.39	1.34
F	0.17	0.16	0.16
Cl	–	0.01	0.01

Note: Standard deviations are given in parentheses.
* From Mössbauer analysis (Scordari et al. 2006).
† From SIMS analysis (Ottolini et al. 2009).

Scattering curves for fully ionized chemical species were used for non-tetrahedral sites, whereas ionized vs. neutral scattering curves were used for Si and O (Hawthorne et al. 1995). Reflections with $I > 3\sigma_I$ were used for the structure refinements. Refined parameters were: scale factor, atomic positions, cations occupancies, and anisotropic atomic displacement parameters. For each crystal except SA1_9, difference-Fourier maps revealed a peak located at the expected position for the hydrogen atom, at ~0.75 Å from the O4 oxygen site. When the H position was included in the last cycles of each refinement, the final difference-Fourier maps became featureless. The relevant details of each structure refinement are reported in Table 1. All structural parameters are close to those previously reported for the SA sample (Scordari et al. 2006; Ventruti et al. 2008). Final atomic coordinates, site occupancies, and anisotropic and isotropic displacement parameters are given in Table 3. Selected bond distances are listed in Table 4, whereas the distortion parameters for micas are reported in Table 5. Mean atomic numbers and octahedral and tetrahedral bond distances are compared to those calculated from chemical analyses using radii from Shannon (1976) and mean anion radii from Kogarko et al. (2005) in Table 6. CIFs are on deposit[1].

Single-crystal X-ray diffraction (XRD) at high temperature

In situ high-temperature single-crystal diffraction investigations were performed using a Philips PW1100 four-circle diffractometer with a point-counter detector and graphite-monochromatized Mo$K\alpha$ radiation (λ = 0.71073 Å). Operating conditions were 55 kV and 30 mA. An in-house constructed U-shaped microfurnace with a K-type thermocouple was used. Crystals were inserted in sealed quartz capillaries (0.5 mm) and maintained in position by quartz wool. A graphite fragment was inserted at ~1.5 cm from the crystal to prevent oxidation of the sample.

First, for each crystal, unit-cell parameters were measured from room temperature (RT) to 500 °C, i.e., below the critical temperature where Fe-oxidation/deprotonation begins (Ventruti et al. 2008), by centering 25 reflections selected at θ = 7.5–15°. At each temperature, prior to measurement, about 30 min were allowed for thermal equilibration. Unit-cell volumes measured are reported in Table 7. Temperature was then increased at ~10 °C/s to the selected set-point: 640 °C for crystal SA1_14n, 650 °C for SA1_5n, 700 °C for SA1_18n, 740 °C for SA1_9, 750 °C for SA_15n, and then maintained until thermal equilibrium was obtained. Under isothermal conditions, unit-cell parameters were measured at 5 min intervals in the early stages of the experiment, longer time intervals as reaction rate slowed, by centering 15–25 reflections at θ = 7.5–15° to monitor temperature-induced Fe-oxidation/deprotonation. Designated reflections of various *hkl* classes, were scanned periodically ($\omega/2\theta$ scan mode; 2.4 °θ scan width; 0.8 °θ/s scan speed) to check for crystal quality of the sample. After completion of deprotonation, reversal experiments were performed on all crystals, except SA1_18n, by measuring changes in lattice parameters from the set point to RT at regular intervals. Finally, an additional heating cycle was performed on crystals SA1_14n and SA1_9 to measure thermal expansions of the deprotonated crystals to 950 °C. These cell-volume values are reported in Table 7, along with heating information.

RESULTS

Figure 1 reports unit-cell volume variations as a function of temperature. During heating from RT to 500 °C, all samples show linear volume expansion because each unit-cell parameter exhibits linear expansion and there is no significant variation of the β angle. Subsequent heating under isothermal conditions between 640–750 °C (see Table 7) causes Fe-oxidation/deprotonation to occur and a sharp decrease of cell volume results. From the observed volume variations (Fig. 1, Table 7) it is apparent that the same degree of deprotonation, within uncertainty, was achieved for all samples, although the length of time differed. After deprotonation, samples remain stable from RT to 950

[1] Deposit item AM-10-050, CIFs. Deposit items are available two ways: For a paper copy contact the Business Office of the Mineralogical Society of America (see inside front cover of recent issue) for price information. For an electronic copy visit the MSA web site at http://www.minsocam.org, go to the *American Mineralogist* Contents, find the table of contents for the specific volume/issue wanted, and then click on the deposit link there.

TABLE 3. Fractional atomic coordinates, equivalent isotropic (Å^2), and anisotropic displacement parameters

Atom	*x/a*	*y/b*	*z/c*	Occupancy	$U_{iso/equiv}$	U_{11}	U_{22}	U_{33}	U_{23}	U_{13}	U_{12}
Sample SA1_9											
K	0.0000	0.5000	0.0000	1.0166(9)	0.0302	0.0292(10)	0.0275(11)	0.0340(12)	0.0000	–0.0063(9)	–0.0000
Mg1	0.0000	0.0000	0.5000	0.7546(7)	0.0110	0.0091(9)	0.0076(9)	0.0172(11)	0.0000	–0.0045(8)	–0.0000
Fe1	0.0000	0.0000	0.5000	0.2454(7)	0.0110	0.0091(9)	0.0076(9)	0.0172(11)	0.0000	–0.0045(8)	–0.0000
Mg2	0.0000	0.33691(17)	0.5000	0.7346(7)	0.0122	0.0079(5)	0.0125(6)	0.0161(7)	0.0000	–0.0021(5)	–0.0000
Fe2	0.0000	0.33691(17)	0.5000	0.2654(7)	0.0122	0.0079(5)	0.0125(6)	0.0161(7)	0.0000	–0.0021(5)	–0.0000
Si	0.07481(17)	0.16700(12)	0.22560(10)	0.9837(10)	0.0103	0.0101 (4)	0.0089(4)	0.0123(4)	–0.0001(6)	–0.0026(3)	–0.0002(5)
O1	0.3293(6)	0.2261(4)	0.1684(3)	1	0.0202	0.0198(13)	0.0239(15)	0.0172(13)	–0.0024(12)	–0.0042(10)	–0.0048(12)
O2	0.0071(9)	0.0000	0.1692(5)	1	0.0202	0.028(2)	0.0134(18)	0.018(2)	–0.0000	–0.0014(17)	–0.0000
O3	0.1307(5)	0.1686(3)	0.3923(3)	1	0.0127	0.0106(10)	0.0126(11)	0.0148(11)	–0.0014(13)	–0.0020(9)	–0.0004(12)
O4	0.1323(8)	0.5000	0.3984(5)	1	0.0132	0.0147(19)	0.0114(18)	0.014(2)	–0.0000	–0.0029(16)	–0.0000
Sample SA1_5n											
K	0.0000	0.5000	0.0000	1.0367(7)	0.0305	0.0307(3)	0.0308(3)	0.0300(3)	–0.0000	–0.0053(2)	–0.0000
Mg1	0.0000	0.0000	0.5000	0.7414(6)	0.0093	0.00826(18)	0.00752(18)	0.0128(2)	–0.0000	–0.00359(13)	–0.0000
Fe1	0.0000	0.0000	0.5000	0.2586(6)	0.0093	0.00826(18)	0.00752(18)	0.0128(2)	–0.0000	–0.00359(13)	–0.0000
Mg2	0.0000	0.33529(4)	0.5000	0.7371(7)	0.0104	0.00683(12)	0.01226(14)	0.01191(14)	–0.0000	–0.00142(9)	–0.0000
Fe2	0.0000	0.33529(4)	0.5000	0.2629(7)	0.0104	0.00683(12)	0.01226(14)	0.01191(14)	–0.0000	–0.00142(9)	–0.0000
Si	0.07513(5)	0.16684(3)	0.22573(3)	0.9780(9)	0.0094	0.00883(10)	0.00902(10)	0.01052(10)	–0.00002(8)	–0.00194(7)	–0.00009(8)
O1	0.33059(16)	0.22562(10)	0.16869(8)	1	0.0187	0.0174(3)	0.0241(4)	0.0152(3)	–0.0031(3)	–0.0042(2)	–0.0061(3)
O2	0.0069(3)	0.0000	0.16939(12)	1	0.0187	0.0266(5)	0.0135(4)	0.0147(4)	–0.0000	–0.0004(4)	–0.0000
O3	0.13087(13)	0.16741(7)	0.39169(7)	1	0.0113	0.0123(3)	0.0112(2)	0.0107(2)	–0.0002(2)	–0.00202(18)	–0.00031(19)
O4	0.13224(19)	0.5000	0.39883(10)	1	0.0124	0.0119(3)	0.0144(4)	0.0110(4)	–0.0000	–0.0017(3)	–0.0000
H	0.116(15)	0.5000	0.320(4)	0.7389(10)	0.09(2)						
Sample SA1_14n											
K	0.0000	0.5000	0.0000	1.0659(5)	0.0309	0.0305(4)	0.0312(4)	0.0309(4)	–0.0000	–0.0054(3)	–0.0000
Mg1	0.0000	0.0000	0.5000	0.7394(4)	0.0102	0.0091(2)	0.0083(2)	0.0140(3)	–0.0000	–0.00399(19)	–0.0000
Fe1	0.0000	0.0000	0.5000	0.2606(4)	0.0102	0.0091(2)	0.0083(2)	0.0140(3)	–0.0000	–0.00399(19)	–0.0000
Mg2	0.0000	0.33601(5)	0.5000	0.7267(4)	0.0113	0.00745(15)	0.01402(19)	0.01212(17)	–0.0000	–0.00120(12)	–0.0000
Fe2	0.0000	0.33601(5)	0.5000	0.2733(4)	0.0113	0.00745(15)	0.01402(19)	0.01212(17)	–0.0000	–0.00120(12)	–0.0000
Si	0.07501(6)	0.16686(4)	0.22558(4)	0.9837(5)	0.0100	0.00918(13)	0.01024(14)	0.01073(13)	–0.00013(12)	–0.00182(10)	–0.00002(11)
O1	0.3298(2)	0.22594(14)	0.16828(11)	1	0.0194	0.0175(4)	0.0251(5)	0.0161(4)	–0.0033(4)	–0.0044(4)	–0.0055(4)
O2	0.0076(3)	0.0000	0.16904(16)	1	0.0192	0.0258(7)	0.0136(6)	0.0164(6)	–0.0000	–0.0007(5)	–0.0000
O3	0.13088(18)	0.16765(11)	0.39154(10)	1	0.0119	0.0119(3)	0.0125(3)	0.0112(3)	–0.0003(3)	–0.0020(3)	–0.0001(3)
O4	0.1320(3)	0.5000	0.39921(14)	1	0.0130	0.0128(5)	0.0147(5)	0.0112(5)	–0.0000	–0.0016(4)	–0.0000
H	0.109(16)	0.5000	0.317(4)	0.7765(5)	0.07(2)						
Sample SA1_15n											
K	0.0000	0.5000	0.0000	1.0330(8)	0.0327	0.0327(5)	0.0326(5)	0.0329(6)	–0.0000	–0.0055(4)	–0.0000
Mg1	0.0000	0.0000	0.5000	0.7479(7)	0.0108	0.0091(4)	0.0078(4)	0.0162(4)	–0.0000	–0.0037(3)	–0.0000
Fe1	0.0000	0.0000	0.5000	0.2520(7)	0.0108	0.0091(4)	0.0078(4)	0.0162(4)	–0.0000	–0.0037(3)	–0.0000
Mg2	0.0000	0.33531(8)	0.5000	0.7429(7)	0.0117	0.0077(2)	0.0133(3)	0.0140(3)	–0.0000	–0.00151(19)	–0.0000
Fe2	0.0000	0.33531(8)	0.5000	0.2571(7)	0.0117	0.0077(2)	0.0133(3)	0.0140(3)	–0.0000	–0.00151(19)	–0.0000
Si	0.07522(9)	0.16690(5)	0.22591(5)	0.9815(10)	0.0110	0.00979(18)	0.00981(19)	0.0136(2)	–0.0001(2)	–0.00239(15)	–0.00014(18)
O1	0.3300(3)	0.22577(18)	0.16855(16)	1	0.0198	0.0172(6)	0.0241(7)	0.0187(6)	–0.0033(6)	–0.0047(5)	–0.0060(5)
O2	0.0080(5)	0.0000	0.1697(2)	1	0.0204	0.0254(10)	0.0161(8)	0.0181(9)	–0.0000	–0.0002(8)	–0.0000
O3	0.1307(2)	0.16748(15)	0.39138(14)	1	0.0127	0.0122(5)	0.0123(5)	0.0137(5)	–0.0001(5)	–0.0026(4)	–0.0002(5)
O4	0.1317(4)	0.5000	0.3987(2)	1	0.0137	0.0118(7)	0.0154(8)	0.0140(8)	–0.0000	–0.0021(6)	–0.0000
H	0.100(17)	0.5000	0.315(4)	0.7984(10)	0.07(3)						
Sample SA1_18n											
K	0.0000	0.5000	0.0000	1.0109(4)	0.0293	0.0290(2)	0.0290(2)	0.0302(2)	–0.0000	–0.00578(18)	–0.0000
Mg1	0.0000	0.0000	0.5000	0.7398(3)	0.0092	0.00790(15)	0.00668(15)	0.01373(17)	–0.0000	–0.00411(12)	–0.0000
Fe1	0.0000	0.0000	0.5000	0.2602(3)	0.0092	0.00790(15)	0.00668(15)	0.01373(17)	–0.0000	–0.00411(12)	–0.0000
Mg2	0.0000	0.33624(3)	0.5000	0.7271(3)	0.0103	0.00625(9)	0.01221(11)	0.01251(11)	–0.0000	–0.00174(8)	–0.0000
Fe2	0.0000	0.33624(3)	0.5000	0.2729(3)	0.0103	0.00625(9)	0.01221(11)	0.01251(11)	–0.0000	–0.00174(8)	–0.0000
Si	0.07499(4)	0.16691(2)	0.22564(2)	0.9782(5)	0.0086	0.00758(7)	0.00779(8)	0.01077(8)	–0.00010(7)	–0.00223(6)	–0.00000(7)
O1	0.32993(13)	0.22590(9)	0.16846(7)	1	0.0180	0.0160(2)	0.0228(3)	0.0161(3)	–0.0029(2)	–0.0049(2)	–0.0058(2)
O2	0.0080(2)	0.0000	0.16946(10)	1	0.0180	0.0245(4)	0.0125(3)	0.0158(4)	–0.0000	–0.0001(3)	–0.0000
O3	0.13066(11)	0.16766(6)	0.39162(6)	1	0.0106	0.01004(18)	0.01052(19)	0.0113(2)	–0.00001(17)	–0.00219(15)	–0.00021(16)
O4	0.13241(16)	0.5000	0.39916(9)	1	0.0114	0.0106(3)	0.0126(3)	0.0110(3)	–0.0000	–0.0019(2)	–0.0000
H	0.101(10)	0.5000	0.318(4)	0.6750(5)	0.06(2)						

Note: Standard deviations are in parentheses.

°C and show linear volume expansion nearly in parallel to the protonated samples. Axial thermal expansions (Figs. 2a–2b) are anisotropic with $\alpha_c \gg \alpha_a$, α_b and anisotropy increases after deprotonation. Mean axial thermal expansion coefficients ratios calculated from these data are $\alpha_a:\alpha_b:\alpha_c = 1.04:1.00:1.27$ [where $\alpha_b = 1.36(2)\cdot10^{-5}$/K] for the protonated samples and $\alpha_a:\alpha_b:\alpha_c = 1.00:1.05:1.83$ [where $\alpha_a = 1.05(2)\cdot10^{-5}$/K] for the deprotonated samples, in good agreement with Ventruti et al. (2008), who also modeled structural modifications occurring as a function of temperature. No significant variation is observed for the β angle with temperature.

Isothermal annealing experiments

Fe-oxidation/deprotonation at high temperature occurs with contraction of unit-cell parameters and cell volume (Fig. 1), as previously reported (e.g., Tutti et al. 2000; Chon et al. 2003, 2006; Ventruti et al. 2008). Variations of unit-cell parameters vs. time under isothermal conditions (Fig. 3) show that the β angle remains constant within uncertainty and this parameter is not plotted in the figures. All other parameters decrease following an exponential curve and reach a plateau in time as a function of temperature and vary from ~10^4 min at 640 °C to <10^3 min at 750 °C. In Figure 4, the cell-volume variations measured at five

TABLE 4. Selected bond distances (Å) for SA samples

	SA1_9	SA1_5n	SA1_14n	SA1_15n	SA1_18n
Tetrahedral layer					
T-O1	1.662(3)	1.6655(8)	1.6647(11)	1.6654(15)	1.6600(7)
T-O1′	1.662(3)	1.6639(9)	1.6657(12)	1.6677(15)	1.6601(7)
T-O2	1.665(2)	1.6648(5)	1.6653(7)	1.6656(10)	1.6594(4)
T-O3	1.680(3)	1.6729(8)	1.6723(10)	1.6696(15)	1.6687(7)
<T-O>	1.667	1.6668	1.6670	1.6671	1.6621
Octahedral layer					
M1-O4 (×2)	2.055(4)	2.0540(10)	2.0544(14)	2.059(2)	2.0473(9)
M1-O3 (×4)	2.097(3)	2.0937(7)	2.0962(10)	2.0972(14)	2.0895(6)
<M1-O>	2.083	2.0805	2.0823	2.0845	2.0754
M2-O4 (×2)	2.027(3)	2.0360(7)	2.0282(10)	2.0366(15)	2.0223(6)
M2-O3 (×2)	2.095(3)	2.0969(7)	2.1010(11)	2.0996(15)	2.0959(6)
M2-O3′ (×2)	2.085(3)	2.0862(7)	2.0875(10)	2.0904(13)	2.0827(6)
<M2-O>	2.069	2.0730	2.0722	2.0755	2.0670
<M-O>	2.074	2.0755	2.0756	2.0785	2.0698
Interlayer					
K-O1 (×4)	2.951(3)	2.9489(9)	2.9499(12)	2.9525(16)	2.9426(7)
K-O1′ (×4)	3.378(3)	3.3869(10)	3.3816(13)	3.3870(17)	3.3738(8)
K-O2 (×2)	2.948(5)	2.9489(13)	2.9510(17)	2.958(2)	2.9468(11)
K-O2′ (×2)	3.392(5)	3.3951(13)	3.3896(18)	3.394(2)	3.3818(11)
<K-O_{inner} >	2.950	2.949	2.950	2.954	2.944
<K-O_{outer} >	3.383	3.390	3.384	3.389	3.376
<K-O>	3.167	3.170	3.167	3.172	3.160

Note: Standard deviations are in parentheses.

TABLE 5. Geometric parameters derived from structure refinements in space group *C*2/*m*

	SA1_9	SA1_5n	SA1_14n	SA1_15n	SA1_18n
t_{tet} (Å)	2.253	2.246	2.245	2.244	2.240
BLD_T	0.342	0.194	0.145	0.097	0.211
V_T (Å^3)	2.382	2.376	2.376	2.377	2.355
TQE	1.0002	1.0002	1.0002	1.0002	1.0002
TAV	0.909	0.702	0.862	0.812	0.713
τ (°)	110.16	110.11	110.20	110.17	110.11
α (°)	9.58	9.64	9.49	9.50	9.47
Δz (Å)	0.008	0.007	0.0071	0.0111	0.0101
D.M. (Å)	0.578	0.574	0.571	0.565	0.569
Ψ_{M1} (°)	59.26	59.12	59.17	59.08	59.15
Ψ_{M2} (°)	59.03	59.00	58.99	58.93	59.00
BLD_{M1}	0.892	0.841	0.903	0.808	0.917
ELD_{M1}	5.424	5.262	5.317	5.211	5.300
BLD_{M2}	1.359	1.190	1.413	1.241	1.435
ELD_{M2}	5.147	5.115	5.113	5.035	5.124
$Shift_{M2}$ (Å)	0.033	0.018	0.025	0.018	0.027
V_{M1} (Å)	11.82	11.79	11.82	11.86	11.71
OQE_{M1}	1.0131	1.0123	1.0126	1.0121	1.0125
OAV_{M1}	42.103	39.883	40.718	39.108	40.423
V_{M2} (Å^3)	11.60	11.68	11.66	11.72	11.57
OQE_{M2}	1.0120	1.0112	1.0118	1.0114	1.0119
OAV_{M2}	38.946	38.023	38.198	36.910	38.386
t_{oct} (Å)	2.129	2.136	2.135	2.142	2.129
t_{int} (Å)	3.399	3.406	3.397	3.410	3.395
$t_{K\text{-}O4}$ (Å)	3.953	3.959	3.961	3.962	3.952

Notes: t_{tet} = tetrahedral sheet thickness calculated from *z* coordinates of basal and apical O atoms; TQE = tetrahedral quadratic elongation (Robinson et al. 1971); TAV = tetrahedral angle variance (Robinson et al. 1971); τ = tetrahedral flattening angle; α = tetrahedral rotation angle (Zvyagin 1957); Δz = departure from co-planarity of the basal O atoms, (Güven 1971); D.M. = dimensional misfit between tetrahedral and octahedral sheets (Toraya 1981); ψ = octahedral flattening angles (Donnay et al. 1964a, 1964b); BLD = bond-length distortions (Renner and Lehmann 1986); ELD = edge-length distortion (Renner and Lehman 1986); $Shift_{M2}$ = off-center shift of the M2 cation defined as the distance between the refined position of cation and the geometrical center of M2 site (coordinates: *x*/*a* = 0.0, *y*/*b* = 0.3333, *z*/*c* = 0.5); OQE= octahedral quadratic elongation (Robinson et al. 1971); OAV = octahedral angle variance (Robinson et al. 1971); t_{oct} = octahedral sheet thickness (Toraya 1981); t_{int} = calculated from the *z* coordinates of basal O atoms; $t_{K\text{-}O4}$ = projection of K-O4 distance along **c***.

working temperatures and normalized to relevant initial values are reported. Exponential fit results are reported in Table 8 for each unit-cell parameter and cell volume.

TABLE 6. Mean atomic numbers (m.a.n., e^-) of cation sites, octahedral and tetrahedral mean distances, as determined by structure refinements (X-ref) and chemical compositions (EMPA)

	SA1_9	SA1_5n	SA1_14n	SA1_15n	SA1_18n
$e^-_{(M1)\ X\text{-}ref}$	15.44	15.62	15.65	15.53	15.64
$e^-_{(M2)\ X\text{-}ref}$	15.72	15.68	15.83	15.60	15.82
$e^-_{(M1+M2)X\text{-}ref}$	46.88	46.98	47.31	46.73	47.28
$e^-_{(M1+M2)\ EMPA}$	48.01	–	48.14	–	47.71
K $e^-_{X\text{-}ref}$	19.32	19.70	20.25	19.63	19.21
K e^-_{EMPA}	19.98	–	19.52	–	19.53
T $e^-_{X\text{-}ref}$	13.77	13.69	13.77	13.74	13.69
T e^-_{EMPA}	13.66	–	13.67	–	13.66
Σ^+	22.51	–	22.57	–	22.44
Σ^-	22.49	–	22.56	–	22.44
$<T\text{-}O>_{X\text{-}ref}$	1.667	1.6668	1.6670	1.6671	1.6621
$<T\text{-}O>_{EMPA}$	1.669	–	1.668	–	1.669
$<M\text{-}O>_{X\text{-}ref}$	2.074	2.0755	2.0756	2.0785	2.0698
$<M\text{-}O>_{EMPA}$	2.072	–	2.070	–	2.073

DISCUSSION

Kinetic analysis

For a solid-state process, the basic equation of homogeneous kinetics $d\alpha/dt = k f(\alpha)$ [where α = degree of conversion, k = rate constant at a given temperature, and $f(\alpha)$ = kinetic model function, usually an empirical function dependent on the mechanism of reaction] can be applied. The selection of the $f(\alpha)$ function is one that best approximates the experimental data but the main disadvantage is that several kinetic models may provide a similar statistical goodness-of-data approximation. Furthermore, the degree of conversion α is often not directly observed by experimental measurements and hence α must be derived from known relationships.

The process object of this study can be expressed by the redox reaction:

$$(Fe^{2+}+OH^-)_{mica} \leftrightarrow (Fe^{3+}+O^{2-})_{mica} + \tfrac{1}{2}H_2\uparrow.$$

The degree of conversion of this reaction is defined as the variation of the OH^- content in the structure, or of the concentration of Fe^{2+} (or the Fe^{2+}/Fe^{3+} ratio). Both parameters are easily measured at RT on quenched samples, for example by IR or Mössbauer spectroscopy; the continuous measurement of OH^- at high temperature is more difficult. In this study, the variations of unit-cell parameters and volume associated with Fe-oxidation/deprotonation in phlogopite at isothermal conditions were measured. These data show a linear correlation between *c*-cell parameter and OH^- groups per formula unit (gpfu) in trioctahedral micas, namely c (Å) = 10.065(16) + 0.125(13) × OH^-, as noted by Ventruti et al. (2008). Ventruti et al. (2008) used data from samples with known H_2O content, iron speciation, and substitution mechanisms. The contraction of the *c* lattice parameter with time was related to loss of protons at the O4 site, and changes over time provided a direct relationship to the decrease of OH^- content. In the kinetic analysis here, the variation of the *c*-cell parameter as the degree of conversion α of the reaction is chosen. Note that cell volume or other lattice directions do not correlate linearly with OH^- content.

A model-independent value of the activation energy E_a related to Fe oxidation/deprotonation is determined from multiple isothermal runs without the knowledge of a physical model by the "isoconversional" method (Friedman 1964; Baitalow et al.

TABLE 7. Unit-cell volumes (Å^3) measured under equilibrium conditions at different temperatures

	SA1_14n	SA1_5n	SA1_18n	SA1_9	SA1_15n
			Before deprotonation		
25 °C	494.2(1.3)	495.8(1.5)	495.4(1.3)	494.9(0.9)	496.4(0.9)
100 °C	–	497.6(1.5)	497.3(1.3)	497.5(1.2)	497.9(0.9)
150 °C	–	–		498.8(0.9)	–
200 °C	498.2(0.9)	499.7(1.5)	499.4(1.3)	499.3(1.0)	500.1(1.0)
250 °C	–	–		500.7(1.0)	–
300 °C	501.1(1.0)	502.2(1.4)	501.9(1.4)	502.1(1.0)	502.2(1.0)
350 °C	503.6(1.3)	–		503.3(1.0)	–
400 °C	503.0(1.0)	504.1(1.5)	503.7(1.2)	504.7(1.1)	504.4(1.0)
450 °C	504.6(0.9)	–		505.7(0.9)	–
500 °C	505.8(1.0)	506.0(1.5)	506.3(1.2)	506.7(1.0)	506.4(0.9)
Isotherm	**640 °C**	**650 °C**	**700 °C**	**740 °C**	**750 °C**
			After deprotonation		
950 °C	–	–	–	509.6(17.5)*	–
900 °C	–	–	–	508.6(9.0)*	–
850 °C	–	–	–	507.2(1.0)*	–
800 °C	506.0(1.5)*	–	–	506.9(1.1)*	–
750 °C	505.2(1.2)	–	–	505.7(1.1)*	505.7(0.6)
700 °C	504.5(1.2)	–	–	504.9(1.1)	505.0(0.8)
650 °C	503.0(1.1)	503.3(1.6)	–	504.0(0.9)	–
600 °C	502.0(1.1)	502.3(1.4)	–	503.1(0.8)	502.9(0.6)
550 °C	–	–	–	502.0(1.0)	–
500 °C	499.5(1.2)	500.4(1.4)	–	500.8(1.1)	501.1(0.6)
400 °C	497.3(1.0)	498.2(1.4)	–	499.2(1.1)	499.2(0.7)
300 °C	495.6(1.0)	496.5(1.4)	–	496.7(1.1)	497.0(0.6)
200 °C	493.4(0.8)	493.9(1.5)	–	494.4(1.3)	494.8(0.7)
100 °C	491.2(1.0)	492.4(1.4)	–	491.8(1.3)	492.6(0.6)
25 °C	488.8(0.8)	491.0(1.5)	–	490.4(1.1)	491.1(0.6)

Notes: Multiple measurements at the same temperature have been omitted. Standard deviations are in parentheses.
* Measured upon re-heating after reversal experiment.

1999). Data where different isothermal runs produce the same degree of conversion α are used to obtain a linear relationship ln t_{ik} vs. $1/T_{ik}$ (notation of Baitalow et al. 1999) with a slope proportional to E_a. This approach converts the kinetic equation written above into its logarithmic form, and assumes the validity of the Arrhenius equation $k = A \exp(-E_a/RT)$. Here, the isoconversional analysis was performed for various *c*-cell parameters vs. time at various temperatures (Fig. 5). Each curve has the same slope indicating that one mechanism, with one activation energy, is involved in the process. From the slopes of the curves, an activation energy of 187(1) kJ/mol is calculated. A preliminary temperature-dependence value for the process was analyzed by an Arrhenius plot determined from the exponential constants obtained for the variation of the *c*-cell parameter with time at the different temperatures (Table 4). The plot (Fig. 6) is linear and the slope is nearly identical to that found by the isoconversional method. In Figure 6, the temperature dependence of each unit-cell parameter and volume are reported for comparison.

Dehydrogenation and Fe^{2+} oxidation occur in phlogopite by a multi-step process: (1) local dissociation of an OH^- group coupled with electron transfer from a neighbor Fe^{2+} according to $Fe^{2+}+H^+ \rightarrow Fe^{3+}+H$; (2) diffusion of H (or H^++e^-) through the tetrahedral ring to the interlayer along which it diffuses to reach the crystallite surface; and (3) near immediate reaction with ambient oxygen to produce H_2O. Rouxhet (1970) assumed the mono-dimensional diffusion of hydrogen along **c*** as a rate-limiting step. Other authors have suggested that, for iron-rich minerals [X_{Fe} = Fe/(Fe+Mg) > 0.08], the kinetics is rate-limited by diffusion of hydrogen atoms, whereas, for lower iron contents, the reaction is slower and controlled by the mobility of electron holes (e.g., Hercule and Ingrin 1999; Carpenter et al. 2000). Here, a one-dimensional diffusion model through two parallel planar sheets, based on Fick's second law (Carlslaw and Jaeger 1959), was applied to the deprotonation process. It is likely that, as hydrogen reaches the interlayer, it easily migrates along the less-dense (001) path. The temporal contraction of the *c*-cell parameter at various temperatures were fit by the following equation:

$$\Delta c(t) = \frac{8}{\pi^2}\sum_{n=0}^{\infty}\frac{1}{(2n+1)^2}\exp\left(\frac{-D\pi^2(2n+1)^2}{L^2}t\right)$$

where $\Delta c(t)$ is *c*-cell parameter variation scaled on the equilibrium

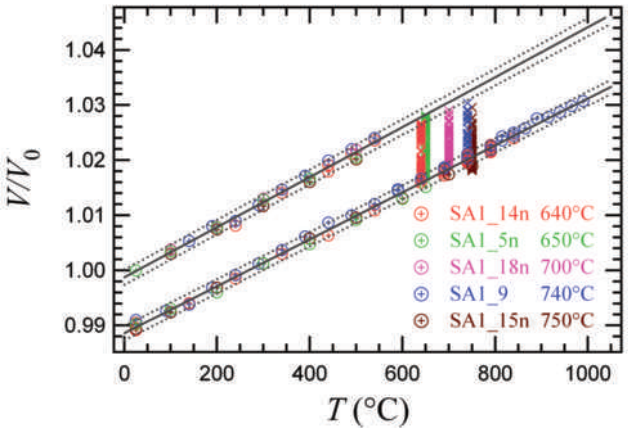

FIGURE 1. Normalized unit-cell volume variations with temperature at isothermal conditions. Linear regressions (solid lines) through all measurements at steady-state conditions are reported with confidence intervals calculated at 95% (dotted lines). Color online.

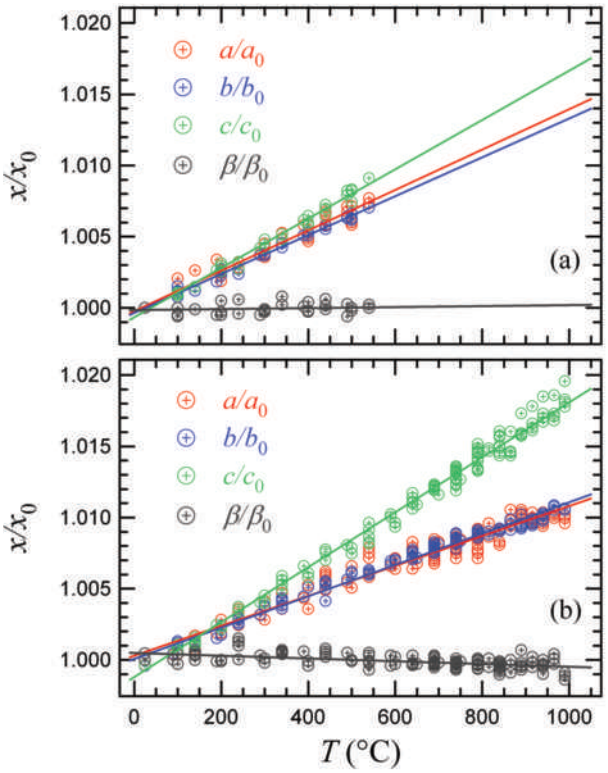

FIGURE 2. Axial thermal expansion of phlogopite SA (**a**) before and (**b**) after deprotonation. Color online.

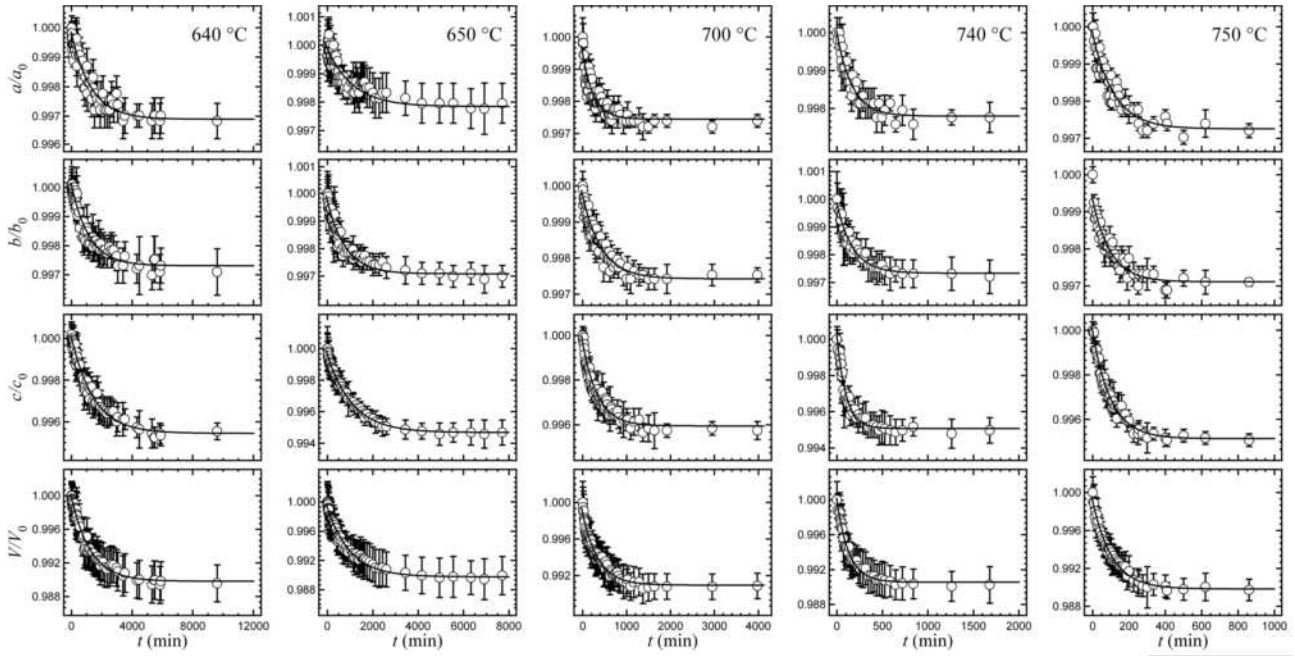

FIGURE 3. Variations of unit-cell parameters as a function of time under isothermal conditions. Working temperatures are shown in the graphs as labels. Exponential fits are reported as solid lines.

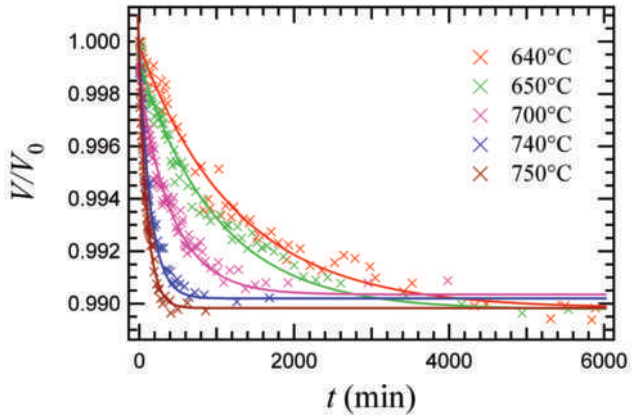

FIGURE 4. Cell-volume variation with time at various temperatures. Exponential fits are reported as solid lines. Same colors as in Figure 1. Color online.

TABLE 8. Unconstrained fit parameters by exponential function $y = K_0 + K_1 \exp(-K_2 * x)$

		a/a_0	b/b_0	c/c_0	V/V_0
640 °C	K_0	0.9969(1)	0.99731(1)	0.99545(9)	0.98982(2)
	K_1	$2.9(1)\cdot10^{-3}$	$2.79(8)\cdot10^{-3}$	$4.61(9)\cdot10^{-3}$	$1.00(2)\cdot10^{-2}$
	K_2	$7.7(8)\cdot10^{-4}$	$8.6(7)\cdot10^{-4}$	$6.8(4)\cdot10^{-4}$	$7.9(4)\cdot10^{-4}$
	χ^2	$5.04\cdot10^{-6}$	$2.95\cdot10^{-6}$	$3.14\cdot10^{-6}$	$1.36\cdot10^{-5}$
650 °C	K_0	0.99784(6)	0.99709(5)	0.99468(4)	0.9898(1)
	K_1	$2.06(8)\cdot10^{-3}$	$2.65(6)\cdot10^{-3}$	$4.96(5)\cdot10^{-3}$	$9.5(1)\cdot10^{-3}$
	K_2	$8.9(9)\cdot10^{-4}$	$1.26(8)\cdot10^{-3}$	$9.1(2)\cdot10^{-4}$	$9.9(4)\cdot10^{-4}$
	χ^2	$5.43\cdot10^{-6}$	$3.56\cdot10^{-6}$	$1.94\cdot10^{-6}$	$1.43\cdot10^{-5}$
700 °C	K_0	0.99745(7)	0.99743(7)	0.99595(7)	0.9910(1)
	K_1	$2.0(1)\cdot10^{-3}$	$2.29(8)\cdot10^{-3}$	$3.70(9)\cdot10^{-3}$	$7.8(2)\cdot10^{-3}$
	K_2	$3.9(5)\cdot10^{-3}$	$2.2(2)\cdot10^{-3}$	$2.9(1)\cdot10^{-3}$	$2.8(2)\cdot10^{-3}$
	χ^2	$4.53\cdot10^{-6}$	$2.56\cdot10^{-6}$	$3.88\cdot10^{-6}$	$1.54\cdot10^{-5}$
740 °C	K_0	0.99780(7)	0.99733(1)	0.99507(8)	0.9905(1)
	K_1	$2.2(1)\cdot10^{-3}$	$2.47(9)\cdot10^{-3}$	$5.0(2)\cdot10^{-3}$	$9.3(2)\cdot10^{-3}$
	K_2	$6.0(7)\cdot10^{-3}$	$5.6(5)\cdot10^{-3}$	$9.9(1)\cdot10^{-3}$	$7.6(4)\cdot10^{-3}$
	χ^2	$1.45\cdot10^{-6}$	$1.22\cdot10^{-6}$	$3.24\cdot10^{-6}$	$7.07\cdot10^{-6}$
750 °C	K_0	0.9973(1)	0.99711(7)	0.99514(8)	0.9898(1)
	K_1	$2.6(1)\cdot10^{-3}$	$2.22(9)\cdot10^{-3}$	$4.8(1)\cdot10^{-3}$	$9.3(2)\cdot10^{-3}$
	K_2	$8.4(9)\cdot10^{-3}$	$1.0(1)\cdot10^{-2}$	$9.9(5)\cdot10^{-3}$	$9.4(4)\cdot10^{-3}$
	χ^2	$2.72\cdot10^{-6}$	$1.85\cdot10^{-6}$	$2.01\cdot10^{-6}$	$6.15\cdot10^{-6}$

Note: Standard deviations are in parentheses.

value at $t \rightarrow \infty$ and normalized, D is the diffusion coefficient, L is sample thickness, and t is time. Because the mono-dimensional diffusion coefficients depend on sample thickness (Tokiwai and Nakashima 2010), the ratio D/L^2 was assumed to be a parameter in the least-squares procedure (Fig. 7). The goodness-of-fit and the superposition of the fitted equations to the isothermal data show that deprotonation in our Fe-bearing sample is described adequately by the one-dimensional diffusion model. The Arrhenius plot (Fig. 8) shows the linear dependence of $\ln(D/L^2)$ on temperature within the analyzed thermal range. The slope yields an activation energy E_a of 195(4) kJ/mol, close to that obtained by the isoconversional method [187(1) kJ/mol]. These E_a values are in good agreement with Rancourt et al. (1993) and their value of 228(2) kJ/mol for oxidation of biotite analyzed by Mössbauer spectroscopy.

Similar to the relationship between c and OH^- determined by Ventruti et al. (2008), a linear relationship between the sheet dimension **b** (or **a** = **b**/√3) and the ratio Fe^{2+}/Fe_{tot} was calculated (Fig. 9). Thus, the b parameter as a function of time and measured at isothermal conditions, relates how **b** changes with Fe^{2+} oxidation. Using the rate coefficients of the linear relationships of c-cell parameter vs. OH^- and b-cell parameter vs. Fe^{2+}/Fe_{tot} to determine the total variation of the b- and c-cell parameters (Δb, Δc), the decrease of Fe^{2+} [$\Delta Fe^{2+} = 0.37(5)$] is close to the value of the hydroxyl group content [$\Delta OH^- = 0.38(4)$]. These results support the hypothesis that Fe^{2+} oxidation occurs simultaneously with deprotonation, as indicated by previous Mössbauer data obtained before and after heating, combined with a single-crystal diffraction study (Ventruti et al. 2008) and HT FTIR measure-

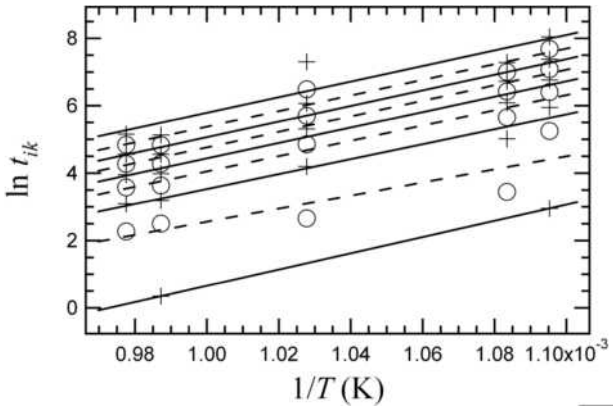

FIGURE 5. Isoconversional plots calculated for various degrees of conversion of *c*-unit cell parameter.

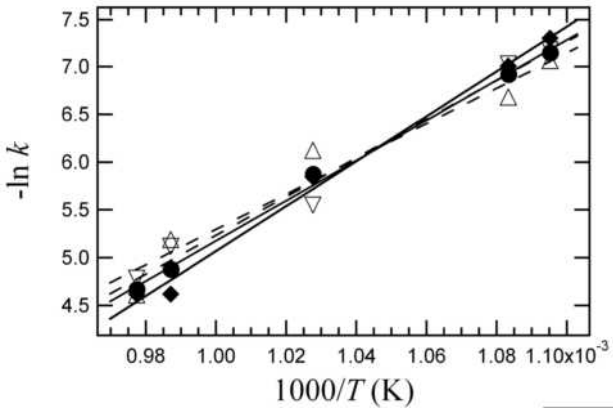

FIGURE 6. Arrhenius plot calculated on the basis of the exponential constants obtained for the variation of unit-cell parameters and volume with time at various temperatures. Circles: cell volume; diamonds: *c*; triangles: *b*; inverted triangles: *a*. The size of the symbols exceeds uncertainty of the measurements. Linear fits are reported as solid lines for *V* and *c*- and dotted lines for *a*- and *b*-cell parameters.

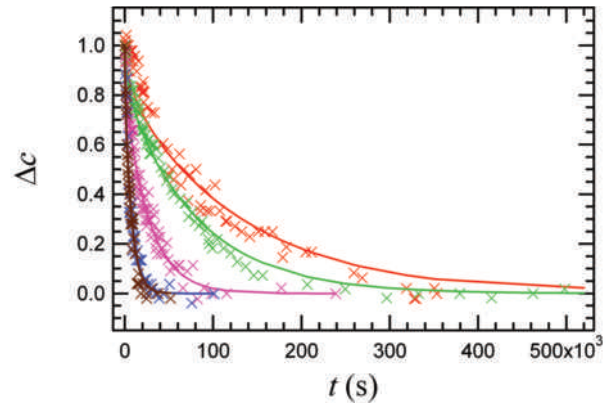

FIGURE 7. Plots of the normalized variations of *c*-cell parameter with time at different temperatures using a one-dimensional diffusion model. Statistical tests R^2 for the models are between 0.88–0.92. Same colors as in Figure 1. Color online.

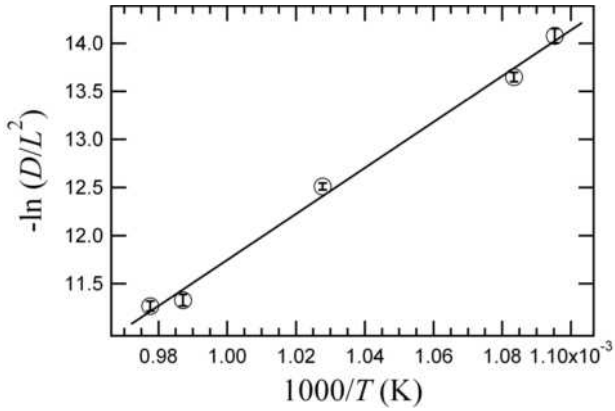

FIGURE 8. Arrhenius plot calculated from the results of the kinetic analysis by the one-dimensional diffusion model. Error bars at 1σ are reported. Linear regression (solid line; R = 0.997) yields an activation energy E_a of 195(4) kJ/mol.

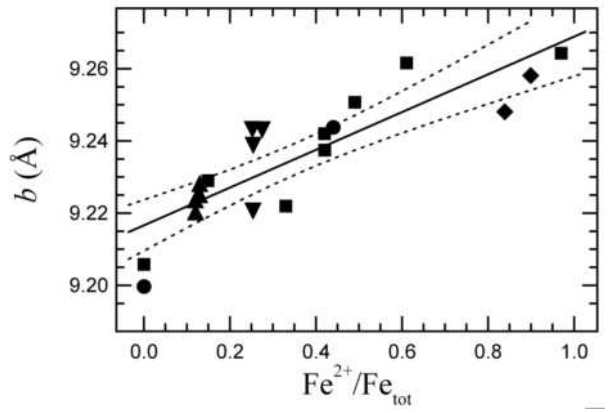

FIGURE 9. Plot of *b*-cell parameter vs. Fe^{2+}/Fe_{tot} content ratio. Solid line represents equation b (Å) = 9.217(3) + 0.052(7) Fe^{2+}/Fe_{tot} obtained by regression analysis on following data: Cesare et al. 2003 (diamonds); Schingaro et al. 2007 (triangles); Matarrese et al. 2008 (inverted triangles); Ventruti et al. 2008 (circles); Lacalamita et al. 2009 (squares). Confidence intervals calculated at 95% are reported as dotted lines.

ments (Lacalamita 2009; Lacalamita et al. 2009). Thus, most Fe^{2+} is octahedrally coordinated to $O_4(OH)_2$. Octahedral sites with compositions (FeO_4F_2) or (FeO_5F) are negligible in support of the iron-fluorine avoidance rule (Munõz 1984), which states that F^- is more readily accommodated in Mg-rich environments, whereas O^{2-} at site O4 is mainly coordinated with Fe^{3+} in $R^{2+}R^{2+}Fe^{3+}$ associations and with Ti^{4+} in $R^{2+}R^{2+}Ti^{4+}$ configuration around O4.

ACKNOWLEDGMENTS

We are particularly indebted to S. Guggenheim for his constructive review and stylistic improvement of the text. The authors are grateful to M. Serracino for assistance during electron probe microanalyses at the IGAG, Istituto di Geologia Ambientale e Geoingegneria, CNR, Rome. This work was supported by grants from the Italian Ministry for University and Research (MIUR).

REFERENCES CITED

Baitalow, F., Schmidt, H.-G., and Wolf, G. (1999) Formal kinetic analysis of processes in the solid state. Thermochimica Acta, 337, 111–120.

Bellotto, M., Gualtieri, A., Artioli G., and Clark., S.M. (1995) Kinetic study of the kaolinite-mullite reaction sequence. Part I: Kaolinite dehydroxylation. Physics

and Chemistry of Minerals, 22, 207–217.
Betteridge, P.W., Carruthers, J.R., Cooper, R.I., Prout, K., and Watkin, D.J. (2003) Crystals version 12: Software for guided crystal structure analysis. Journal of Applied Crystallography, 36, 1487–1492.
Blessing, R.H. (1995) An empirical correction for absorption anisotropy. Acta Crystallographica A, 51, 33–38.
Brigatti, M.F. and Guggenheim, S. (2002) Mica crystal chemistry and the influence of pressure, temperature, and solid solution on atomistic models. In A. Mottana, F.P. Sassi, J.B. Thompson, and S. Guggenheim, Eds., Micas, 46, p. 1–97. Reviews in Mineralogy and Geochemistry. Mineralogical Society of America, Chantilly, Virginia.
Bruker (2004a) AXS APEX2 Release 1.1.2.2; Bruker Molecular Analysis Research Tool, Bruker AXS Inc., Madison, U.S.A.
——— (2004b) SAINT-IRIX Release 7.12A. Integration Software for Single Crystal Data. Bruker AXS Inc., Madison, U.S.A.
Carlslaw, H.S. and Jaeger, J.C. (1959) Conduction of heat in solids, 510 p. Clarendon, Oxford, U.K.
Carpenter, S.J., Mackwell, S.J., and Dyar, M.D. (2000) Hydrogen in diopside diffusion profiles. American Mineralogist, 85, 480–488.
Cesare, B., Cruciani, G., and Russo, U. (2003) Hydrogen deficiency in Ti-rich biotite from anatectic metapelites (El Joyazo, SE Spain): Crystal-chemical aspects and implications for high-temperature petrogenesis. American Mineralogist, 88, 583–595.
Chon, C-M., Kim, S.A., and Moon, H-S. (2003) Crystal structures of biotite at high temperatures and of heat-treated biotite using neutron powder diffraction. Clays and Clay Minerals, 51, 519–528.
Chon, C-M., Lee, C-K., Song, Y., and Kim, S.A. (2006) Structural changes and oxidation of ferroan phlogopite with increasing temperature: in situ neutron powder diffraction and Fourier transform infrared spectroscopy. Physics and Chemistry of Minerals, 33, 289–299.
Comodi, P., Zanazzi, P.F., Weiss, Z., Rieder, M., and Drábek, M. (1999) "Cs-tetraferri-annite:" High-pressure and high-temperature behavior of a potential nuclear waste disposal phase. American Mineralogist, 84, 325–332.
Donnay, G., Morimoto, N., Takeda, H., and Donnay, J.D.H. (1964a) Trioctahedral one-layer micas. I. Crystal structure of a synthetic iron mica. Acta Crystallographica, 17, 1369–1373.
Donnay, G., Donnay, J.D.H., and Takeda, H. (1964b) Trioctahedral one-layer micas. II. Prediction of the structure from composition and cell dimensions. Acta Crystallographica, 17, 1374–1381.
Ferrow, E. (1987) Mössbauer and X-ray studies on the oxidation of annite and ferriannite. Physics and Chemistry of Minerals, 14, 270–275.
Friedman, H.L. (1964) Kinetics of thermal degradation of char-forming plastics from thermogravimetry. Application to a phenolic plastic. Journal of Polymer Science, C6, 183–195.
Guggenheim, S., Chang, Y.H., and Koster van Groos, A.F. (1987) Muscovite dehydroxylation: High-temperature studies. American Mineralogist, 72, 537–550.
Güven, N. (1971) The crystal structure of $2M_1$ phengite and $2M_1$ muscovite. Zeitschrift für Kristallographie, 134, 196–212.
Hawthorne, F.C., Ungaretti, L., and Oberti, R. (1995) Site populations in minerals: Terminology and presentation of results. Canadian Mineralogist, 33, 907–911.
Hercule, S. and Ingrin, J. (1999) Hydrogen in diopside: Diffusion, kinetics of extraction-incorporation, and solubility. American Mineralogist, 84, 1577–1587.
Hogg, C.S. and Meads, R.E. (1975) A Mössbauer study of thermal decomposition of biotites. Mineralogical Magazine, 40, 79–88.
Ingrin, J. and Skogby, H. (2000) Hydrogen in nominally anhydrous upper-mantle minerals: Concentration levels and implications. European Journal of Mineralogy, 12, 543–570.
Kogarko, L.N., Uvarova, Y.A., Sokolova, E., Hawthorne, F.C., Ottolini, L., and Grice, J.D. (2005) Oxykinoshitalite, a new mica from Fernando-de-Norohna Island, Brazil: Occurrence and crystal structure. Canadian Mineralogist, 43, 1501–1510.
Lacalamita, M. (2009) Chemical and structural study of anionic and cationic sites in trioctahedral micas at RT and HT temperatures. Plinius, 35, 134–139.
Lacalamita, M., Scordari, F., and Ventruti, G. (2009) Room and high temperature micro-FTIR and SCXRD study of Fe-rich phlogopites. Geoitalia 2009—VII Forum Italiano di Scienze della Terra, Rimini, Epitome 3, W3-54.
Matarrese, S., Schingaro, E., Scordari, F., Stoppa, F., Rosatelli, G., Pedrazzi, G., and Ottolini, L. (2008) Crystal chemistry of phlogopite from Vulture-S. Michele subsynthem volcanics (Mt. Vulture, Italy) and volcanological implications. American Mineralogist, 93, 426–437.
Mazzucato, E., Artioli, G., and Gualtieri, A. (1999) High temperature dehydroxylation of muscovite-$2M_1$: A kinetic study by in situ XRPD. Physics and Chemistry of Minerals, 26, 375–381.
Munõz, J.L. (1984) F-OH and Cl-OH exchange in micas with application to hydrothermal deposits. In S.W. Bailey, Ed., Micas, 13, p. 469–493. Reviews in Mineralogy, Mineralogical Society of America, Chantilly, Virginia.
Ohta, T., Takeda, H., and Takéuchi, Y. (1982) Mica polytypism: Similarities in the crystal structures of coexisting $1M$ and $2M_1$ oxybiotite. American Mineralogist, 67, 298–310.
Ottolini, L., Schingaro, E., Scordari, F., Mesto, E., and Matarrese, S. (2009) The role of SIMS in the investigation of the complex crystal-chemistry of mica minerals. Geoitalia 2009—VII Forum Italiano di Scienze della Terra, Rimini, Epitome 3, W3-59.
Pouchou, J.-L. and Pichoir, F. (1985) "PAP" $\Phi(\rho Z)$ procedure for improved quantitative micro-analysis. Microbeam Analysis, 104–160.
Rancourt, D.G., Tume, P., and Lalonde, A.E. (1993) Kinetics of the $(Fe^{2+}+OH^-)_{mica} \rightarrow (Fe^{3+}+O^{2-})_{mica}+H$ oxidation reaction in bulk single-crystal biotite studied by Mossbauer spectroscopy. Physics and Chemistry of Minerals, 20, 276–284.
Redfern, S.A.T. (1987) The kinetics of dehydroxylation of kaolinite. Clay Minerals, 22, 447–456.
Renner, B. and Lehmann, G. (1986) Correlation of angular and bond length distortions in TO_4 units in crystals. Zeitschrift für Kristallographie, 175, 43–59.
Robinson, K., Gibbs, G.V., and Ribbe, P.H. (1971) Quadratic elongation, a quantitative measure of distortion in coordination polyhedra. Science, 172, 567–570.
Rouxhet, P.G. (1970) Kinetics of dehydroxylation and of OH-OD exchange in macrocrystalline micas. American Mineralogist, 55, 841–853.
Russell, R.L. and Guggenheim, S. (1999) Crystal structure of near-end-member phlogopite at high temperatures and heat-treated Fe-rich phlogopite: The influence of the O, OH, F site. Canadian Mineralogist, 37, 711–720.
Sanz, J., Gonzales-Carreno, T., and Gancedo, R. (1983) On dehydroxylation mechanism of a biotite in vacuo and in oxygen. Physics and Chemistry of Minerals, 9, 14–18.
Schingaro, E., Matarrese, S., Scordari, F., Rosatelli, G., Stoppa, F., and Pedrazzi, G. (2007) Phlogopite crystal chemistry of trioctahedral micas from the Ventaruolo subsynthem volcanics (Mt. Vulture, Italy): A multi-method study. Mineralogical Magazine, 71, 519–537.
Scordari, F., Ventruti, G., Sabato, A., Bellatreccia, F., Della Ventura, G., and Pedrazzi, G. (2006) Ti-rich phlogopite from Mt. Vulture (Potenza, Italy) investigated by a multianalytical approach: Substitutional mechanisms and orientation of the OH dipoles. European Journal of Mineralogy, 18, 379–391.
Shannon, R.D. (1976) Revised effective ionic radii and systematic studies of interatomic distances in halides and chalcogenides. Acta Crystallographica, A32, 751–767.
Sheldrick, G.M. (2004) SADABS, Program for Empirical Absorption Correction of Area Detector Data. University of Göttingen, Germany.
Sundvall, R., Skogby, H., and Stalder, R. (2009) Dehydration-hydration mechanisms in synthetic Fe-poor diopside. European Journal of Mineralogy, 21, 17–26.
Takeda, H. and Morosin, B. (1975) Comparison of observed and predicted structural parameters of mica at high temperature. Acta Crystallographica B, 31, 2444–2452.
Takeda, H. and Ross, M. (1975) Mica polytypism: dissimilarities in the crystal structures of coexisting $1M$ and $2M_1$ biotite. American Mineralogist, 60, 1030–1040.
Tokiwai, K. and Nakashima, S. (2010) Dehydration kinetics of muscovite by in situ infrared microspectroscopy. Physics and Chemistry of Minerals, 37, 91–101.
Toraya, H. (1981) Distortions of octahedra and octahedral sheets in $1M$ micas and the relation to their stability. Zeitschrift für Kristallographie, 157, 173–190.
Tsvetkov, A.I. and Val'yashikhina, E.P. (1956) Concerning hydration and oxidation of micas. Izvestia Akademii Nauk SSSR, Seria Geologitcheskaja, 5, 74–88.
Tutti, F., Dubrovinsky, L.S., and Nygren, M. (2000) High-temperature study and thermal expansion of phlogopite. Physics and Chemistry of Minerals, 27, 599–603.
Vedder, W. and Wilkins, R.W.T. (1969) Dehydroxylation and rehydroxylation, oxidation and reduction of micas. American Mineralogist, 54, 482–509.
Ventruti, G., Zema, M., Scordari, F., and Pedrazzi, G. (2008) Thermal behavior of a Ti-rich phlogopite from Mt. Vulture (Potenza, Italy): An in situ X-ray single crystal diffraction study. American Mineralogist, 93, 632–643.
Ventruti, G., Levy, D., Pavese, A., Scordari, F., and Suard, E. (2009) High-temperature treatment, hydrogen behaviour and cation partitioning of a Fe-Ti bearing volcanic phlogopite by in situ neutron powder diffraction and FTIR spectroscopy. European Journal of Mineralogy, 21, 385–396.
Vielzeuf, D. and Schmidt, M.W. (2001) Melting relations in hydrous systems revisited: application to metapelites, metagreywackes, and metabasalts. Contributions to Mineralogy and Petrology, 141, 251–267.
Virgo, D. and Popp, R.K. (2000) Hydrogen deficiency in mantle-derived phlogopites. American Mineralogist, 85, 753–759.
Zanazzi, P.F. and Pavese, A. (2002) Behavior of micas at high pressure and high temperature. In A. Mottana, F.P. Sassi, J.B. Thompson, and S. Guggenheim, Eds., Micas, 46, p. 99–116. Reviews in Mineralogy and Geochemistry, Mineralogical Society of America, Chantilly, Virginia.
Zeng, Y., Feng, Z., and Hao, J. (1990) Interaction between biotite and Na-Ca-chloride fluid at 500 °C and 1 kbar. Neues Jahrbuch für Mineralogie, Monatshefte, 11, 517–520.
Zvyagin, B.B. (1957) Determination of the structure of celadonite by electron diffraction. Soviet Physics Crystallography, 2, 388–394.

Manuscript received February 5, 2010
Manuscript accepted May 16, 2010
Manuscript handled by Grant Henderson